Controllable Tuning Plasmonic Coupling with Nanoscale Oxidation

Tao Ding, Daniel Sigle, Liwu Zhang,† Jan Mertens, Bart de Nijs, and Jeremy Baumberg*

Nanophotonics Centre, Cavendish Laboratory, University of Cambridge, Cambridge CB3 0HE, U.K. †Present address: L.Z.: Department of Environmental Science and Technology, Fudan University, No. 220 Handan Rd., Shanghai 200433, P.R. China.

ABSTRACT The nanoparticle on mirror (NPoM) construct is ideal for the strong coupling of localized plasmons because of its simple fabrication and the nanometer-scale gaps it offers. Both of these are much harder to control in nanoparticle dimers. Even so, realizing controllable gap sizes in a NPoM remains difficult and continuous tunability is limited. Here, we use reactive metals as the mirror so that the spacing layer of resulting metal oxide can be easily and controllably created with specific thicknesses resulting in continuous tuning of the plasmonic coupling. Using Al as a case study, we contrast different approaches for oxidation including electrochemical oxidation, thermal annealing, oxygen plasma treatments, and photo-oxidation by laser irradiation. The thickness of the oxidation layer is calibrated with depth-mode X-ray photoemission spectroscopy (XPS). These all consistently show that increasing the thickness of the oxidation layer blue-shifts the plasmonic resonance peak while the transverse mode remains constant, which is well matched by simulations. Our approach provides a facile and reproducible method for scalable, local and controllable fabrication of NPoMs with tailored plasmonic coupling, suited for many applications of sensing, photochemistry, photoemission, and photovoltaics.

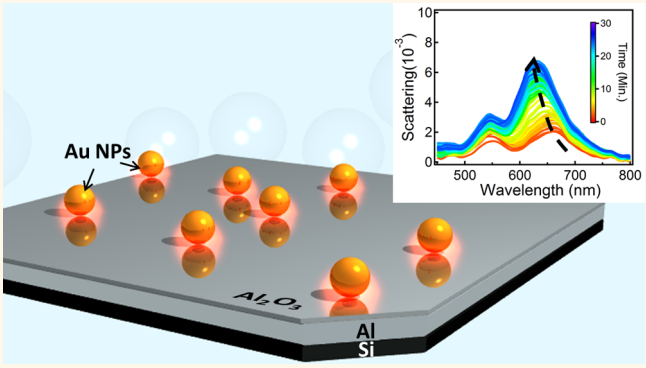

KEYWORDS: electrochemistry · aluminum · plasmons · oxidization · irradiation

Strongly coupled plasmonic systems have attracted tremendous attention because of the strong electric fields confined in nanoscale volumes, which provide significant enhancement effects for applications in surface-enhanced Raman scattering (SERS), photoemission, and photovoltaics.[1−4] Most of the nanoassembled strongly coupled constructs are large cross-section nanostructures with nano- and sub-nanosize internal voids into which strong fields can be confined. Such plasmonic coupled system can be classified into metal nanoparticle−nanoparticle coupling,[5] metal nanoparticle−film coupling (nanoparticle on mirror, NPoM),[6] and periodic metallic coupled systems.[7−10] For nanoparticle−nanoparticle systems, the yield and consistency of these synthetic plasmonic nanostructures are sub-optimal, compromising the reproducibility of SERS. This is similar for lithographically defined plasmonic constructs, which cannot provide reliable nm-scale gaps in cost-effective manner. The nanoparticle on mirror construct is one of the best controlled plasmonic systems, as it can be easily made by depositing monodisperse metal nanoparticles onto metal films: strong interactions between a NP and its image charges form a dimer-like construct. This coupling between NP and metallic film is strongly dependent on the shape of the nanoparticles, the dielectric constant of the medium, and the distance between the NP and the metal film surface. Based on this coupled system, various *in situ* applications have been trialed, with biomolecules,[11,12] chemical reactions,[13] and phonon modes[14] all detected by SERS.

Most of the NPoM systems so far investigated are based on Au or Ag NPs on a Au mirror,[6,11−20] while the spacer materials include polymers,[6] ligands,[15,16] 2D materials,[17,18] and deposited oxide layers,[19] all of which are static and cannot easily be continuously tuned. However, as well as Au, metallic films including Al, Cu, and Ag could also elicit image charges from NPs to form dimer-like coupled systems. Moreover, these can all easily form oxidized layers on top of the

* Address correspondence to jjb12@cam.ac.uk.

Received for review February 27, 2015 and accepted May 15, 2015.

Published online May 15, 2015
10.1021/acsnano.5b01283

metal surface so that the spacing between the Au NPs and metal films can be tunable as long as the oxidation process is well controlled.[20] In this way, we can monitor and control the plasmonic coupling to make tunable plasmonic antennae and SERS sensors.

In this article, we use Al mirrors as a case study to demonstrate such controllable and tunable plasmonic coupling, as these can be easily modified through electrochemical oxidation.[20] We extend the previous approach[20] to show in-depth studies of several means of controlled oxidation at the nanoscale including direct laser photo-oxidation of selected NPoMs, and thus making this technique highly versatile. We find the Al films exhibit similar coupling effects to Au mirrors, but build an oxide layer underneath the NPs. With the surface of Al metal always covered with 1−2 nm Al_2O_3, further oxidation of the whole Al film is retarded.[21] This oxidative layer also functions as a dielectric spacer for the metallic NPs (here Au) on top. By fine-tuning the thickness of the oxidized layer under appropriate conditions, Au NPs on Al mirror with different spacing can be obtained revealing changes of plasmonic coupling that are monitored with single nanoparticle scattering spectroscopy.

RESULTS AND DISCUSSION

To construct these samples, 50 nm thick Al films were coated onto Si wafers *via* e-beam evaporation (rate 1 Å/s, vacuum 10^{-6} Torr, Lesker). Because the surface plasmon depth for Al is less than 10 nm, this thickness is not critical as long as it exceeds 20 nm (Supporting Information Figure S1). In the following, we always use substrates with 50 nm Al films unless stated otherwise. We first verify the plasmonic coupling between Au NPs (obtained from BBI) and these Al mirrors, by drop-casting NPs of different sizes. The colors of the resulting Au NPoMs from dark field scattering with objective lens NA = 0.8 are clearly size dependent (Figure 1a−c). With increasing diameter of Au NPs from 60 to 100 nm, their NPoM color changes from yellow-green to red to orange while for the same NPs on Si wafers (Figure 1d−f) it barely changes. This confirms that the color is dominated by the longitudinal coupling between Au NP and Al films rather than any particle size-induced shift of the transverse mode. These spectra were recorded with 20 randomly selected Au NPs on the Al mirror and subsequently averaged (Supporting Information Figure S2). The averaged scattering spectra (Figure 1g) show the dipolar resonance peak red-shifting with increasing size of Au NPs, while for the Au NPs on Si substrate no significant shift is seen (Figure 1i), summarized in the spectral shifts extracted in Figure 1h, j. With increasing NP size, the quadrupolar coupled plasmon[22] peak around 524 nm (dashed, Figure 1g) also becomes more prominent (though it overlaps also with the transverse plasmon mode). Because the scattering cross-section of such nanoparticle constructs scales (in a simplified picture) as $\sim R^6$, where R is the nanoparticle radius, this results in a strong size dependence. Compared to boundary-element method (BEM) simulations mapping the coupling between Au NPs and Al mirror (Figure 1h, blue and green dashed lines), we conclude that the thickness of the native dielectric oxide layer on the as-grown Al metal films is 2 ± 0.5 nm, which is consistent with previous reports.[23,24]

It is well-known that such a dense oxide layer on Al films can stop further oxidation of the metal while its thickness is dependent on the synthesis conditions and environmental factors including temperature and humidity.[25] To ensure consistent experimental results, all the Al films were evaporated under high vacuum (10^{-6} Torr) and stored under a dry nitrogen atmosphere. Nevertheless, the thin ~2 nm layer of Al_2O_3 always forms on top of these Al films.

Developing a controllable way of oxidizing the Al films is thus crucial to fine-tune the plasmonic coupling between Au NPs and Al mirror. First, we perform electrochemical oxidation, which allows us to observe *in situ* the increasing thickness of the oxide layer through the shift of plasmonic coupling under dark-field microscopy (Figure 2a). The electrochemical oxidation is carried out at a potential of 4 V in an acetic acid (AcOH, 0.1 M) aqueous solution. A glass coverslip caps the electrolyte liquid surface to ensure good optical surfaces enabling high resolution observation. In air, the 100 nm Au NPs on Al mirror appear bright orange under dark field (Figure 1c), however when immersed in AcOH solution, the scattered color of the Au NPs changes to green (Figure 2b, left image). The coupled dipole mode is slightly red-shifted and the quadrupolar mode is enhanced in the solvent (Figure 2c), probably due to its infiltration into the slightly porous matrix. The green quadrupolar mode now dominates the observed color only because of the lower NA objectives needed to be compatible with this cell architecture (and which thus collects less of the high angle coupled plasmon mode emission).[26] As the electrochemical reaction proceeds, the scattering color gradually turns from green to red to orange (Figure 2b, middle and right) as the longitudinal coupled mode blue-shifts into the visible with increasing intensity (Figure 2c). The spectral changes for a typical Au NP with oxidation time (Figure 2c) reveal the evolution of coupling wavelength (from 675 to 628 nm) and scattering intensity (from 0.8% to 2.5%) within 30 min (Figure 2d). The increasing thickness of oxide progressively decouples the dipolar plasmons, producing the saturating blue-shift. The surface morphology of Au NPs on Al before and after electrochemical oxidation (Figure 2e, f) shows dark regions on the surface which suggest an increase in roughness from formation of a thicker oxidation layer within the Al films.[27] The increase of scattering intensity arises from better in/out-coupling

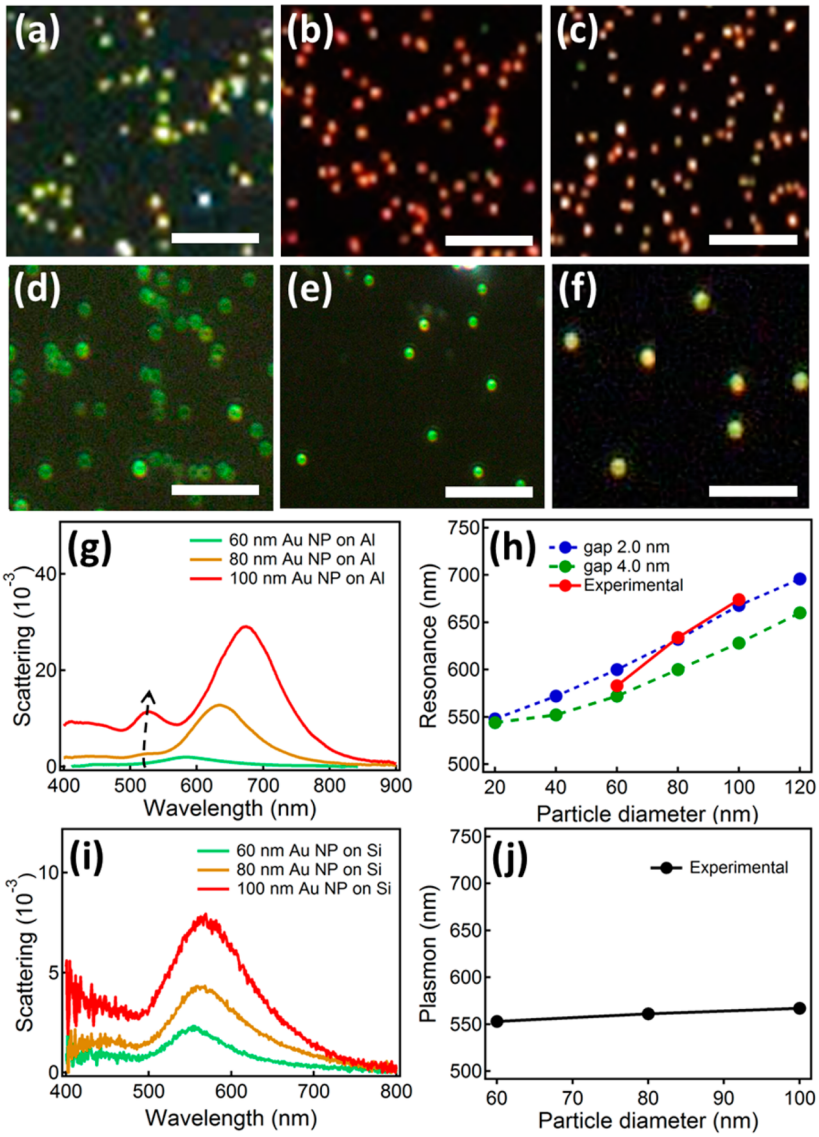

Figure 1. Dark field images of different sized Au NPs on Al mirror (a−c) and Si wafer (d−f). (a, d) 60 nm, (b, e) 80 nm, (c, f) 100 nm. Scale bars are 10 μm. (g, i) Scattering spectra of different sized Au NPs on (g) Al films and (i) Si wafers, with peak positions extracted in panels (h) and (j). The blue and green dashed lines in panel h are the simulated resonance positions for gap sizes of 2 and 4 nm Al_2O_3.

for thicker gaps (due to better matching to radiating photons which is reduced in nm-scale gaps, Supporting Information Figure S15).

To further confirm the effect of oxidation-induced increases in gap thickness between Au NPs and Al films, thermal oxidation was also used to oxidize the films to different extents. We anneal the Al films at temperatures ranging from 300 to 850 K for 10 min, subsequently taking scattering spectra (Supporting Information Figure S3) of the Au NPs on these annealed Al films in air (Figure 3a). With increasing temperature, the resonance peak progressively blue-shifts while the transverse mode at 524 nm remains unchanged. The increased scattering background is mainly due to the roughening of the Al surface at higher annealing temperatures. To examine the composition changes of the annealed Al films, EDX elemental analysis is performed (Supporting Information Figure S4), which shows Si peaks because the signal collection depth reaches down to the Si substrate. The EDX shows progressive increases of the oxygen peak with increasing annealing temperature, quantitatively reflecting the increasing thickness of the Al_2O_3 layers. As the annealing temperature is increased to 850 K (Figure 3b, black line), the atomic ratio between O and Al rises to 1.5, which means the entire Al film is transformed into the dielectric Al_2O_3. Correspondingly, a clear blue-shift of the plasmon resonance peak is observed from 669 to 587 nm, as the NPoM reverts to a dielectric loaded single NP resonance (Figure 3b, blue line).

A third controllable oxidation route is employed by exposing the Al films to oxygen plasma for different times. Scattering spectra of Au NPs on these plasma-treated substrates (Supporting Information Figure S5)

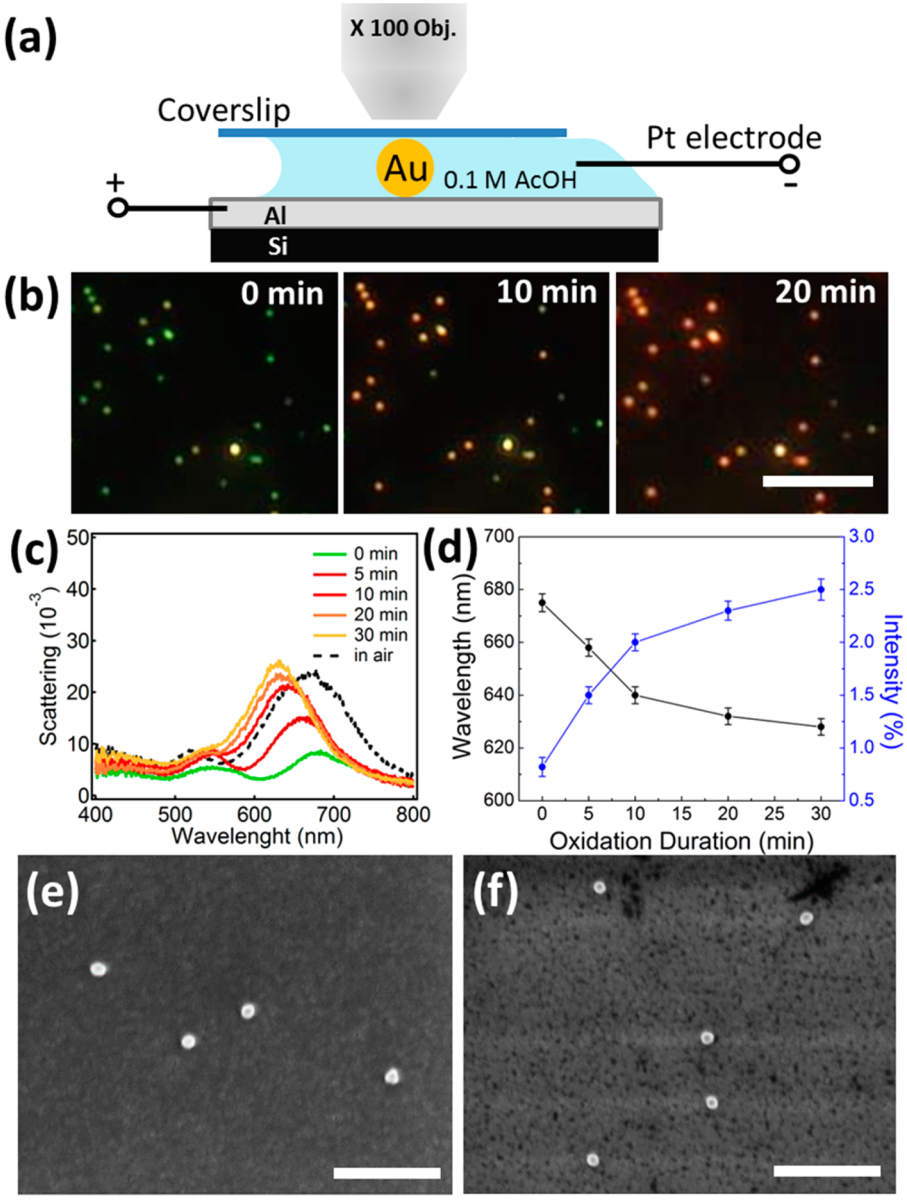

Figure 2. (a) Schematic illustration of the setup for *in situ* observation of Au NPs on Al mirror under electrochemical oxidation. (b) Dark field images of Au NPs on Al mirror immersed in AcOH (0.1 M) electrolyte for electrochemical oxidation of 0, 10, and 20 min. Scale bar is 10 μm. (c) Corresponding scattering spectra of a typical Au NP on Al mirror collected after different times of electrochemical oxidation, dashed line shows Au NP on Al mirror before immersing in AcOH. (d) Change of wavelength and intensity with oxidation time. (e, f) SEM images of Au NPs on Al mirror before (e) and after (f) 30 min electrochemical oxidation. Scale bars are 1 μm.

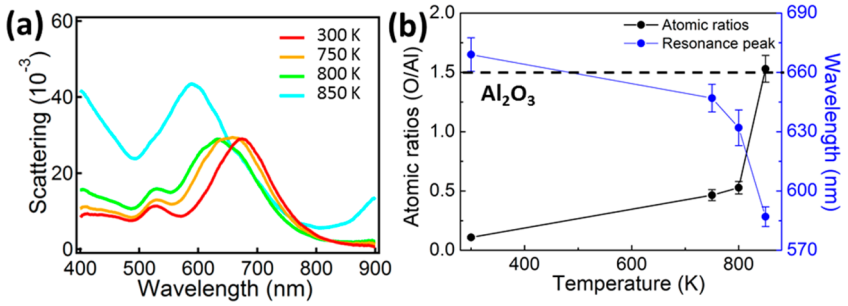

Figure 3. (a) Scattering spectra of Au NPs on Al mirrors which have been annealed for 10 min at different temperatures. (b) Correlation between elemental composition of the Al/Al_2O_3 films and the resonance wavelength of Au NPoMs at different annealing temperatures.

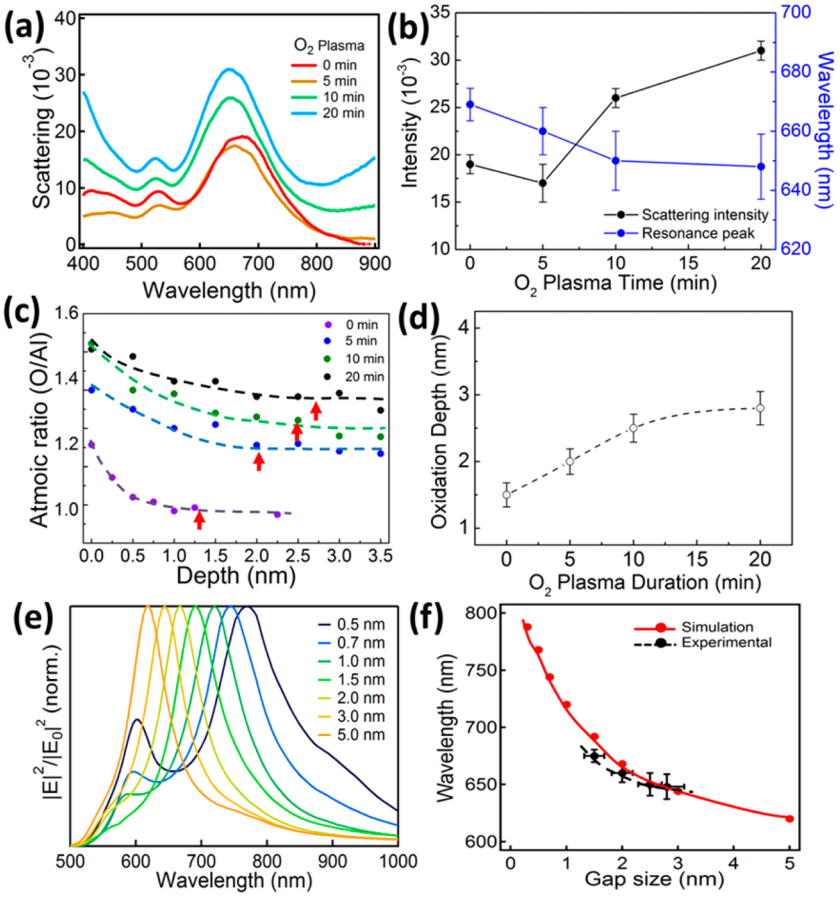

Figure 4. (a) Scattering spectra of Au NPs on Al mirrors which are pretreated with oxygen plasma for different durations. (b) Changes of resonance wavelength and intensity with different plasma oxidation time. (c, d) XPS analysis of the elemental composition of Al films with different plasma treatment times for in-depth mode. (c) Changes of atomic ratio between O and Al at different depths of the films. Red arrows indicate saturation. (d) Estimated oxidation depth (from XPS) of Al films after oxygen plasma with different duration. Dashed line serves as guide to eye only. (e) Simulated enhanced local field spectra with different gap sizes, and (f) extracted peak resonance wavelengths (red solid line) correlated with experimental values (black dashed line).

are averaged and shown in Figure 4a. The oxygen plasma should enhance the oxide layer on top of the Al films becoming thicker with longer plasma treatment. However, because the O_2 plasma treatment produces a thinner Al_2O_3 film compared to thermal annealing, only a small blue shift of the resonance peak is observed from 675 to 648 nm (Figure 4b). The increase of averaged background scattering intensity is again due to the roughening of the Al films after the plasma treatment. The surface composition of the Al films was characterized with XPS in depth mode to quantitatively determine the thickness of the Al_2O_3 layers (Supporting Information Figures S6−S9). The signal from XPS was collected with 5 accumulations for each layer, measuring elemental Al and O. After each layer, a focused ion beam (500 V) was applied to etch the surface layer for 10 s at a rate of ~0.05 nm/s. As summarized in Figure 4c, the atomic ratio between O and Al gradually decreases with depth inside the Al films eventually saturating at the bulk layer of Al. Because the probing depth of XPS is around 10 nm and oxygen contamination is also introduced during the ion milling process, the ratio between O and Al is not zero, even when it reaches the bulk Al layer. Longer plasma treatments, which inject more oxygen atoms into the Al films, seem to exacerbate this artifact, probably because they induce more local damage which increases the oxygen diffusion and contamination deeper into the bulk. However, we obtain a rough estimate of the thickness of the oxide layer using the observed kink (indicated with red arrows in Figure 4c) at saturation. For Al films treated with longer plasma times, the ratio of O:Al is larger and the thickness of Al_2O_3 increases (Figure 4d), saturating after 10 min of plasma treatment. This is because plasma oxidation is a surface activated process, so that the dense Al_2O_3 layer formed on top of the Al will then stop penetration of O_2^- into the underlying Al film, producing a self-limiting oxide layer.[28] The thickness of Al_2O_3 measured in this way can be correlated with the wavelength of the resonance in Figure 4b (Figure 4f, black dashed line). We also show the simulated wavelengths of coupled Au NPs on Al mirrors extracted from the resonances in the simulated spectra (Figure 4e) for

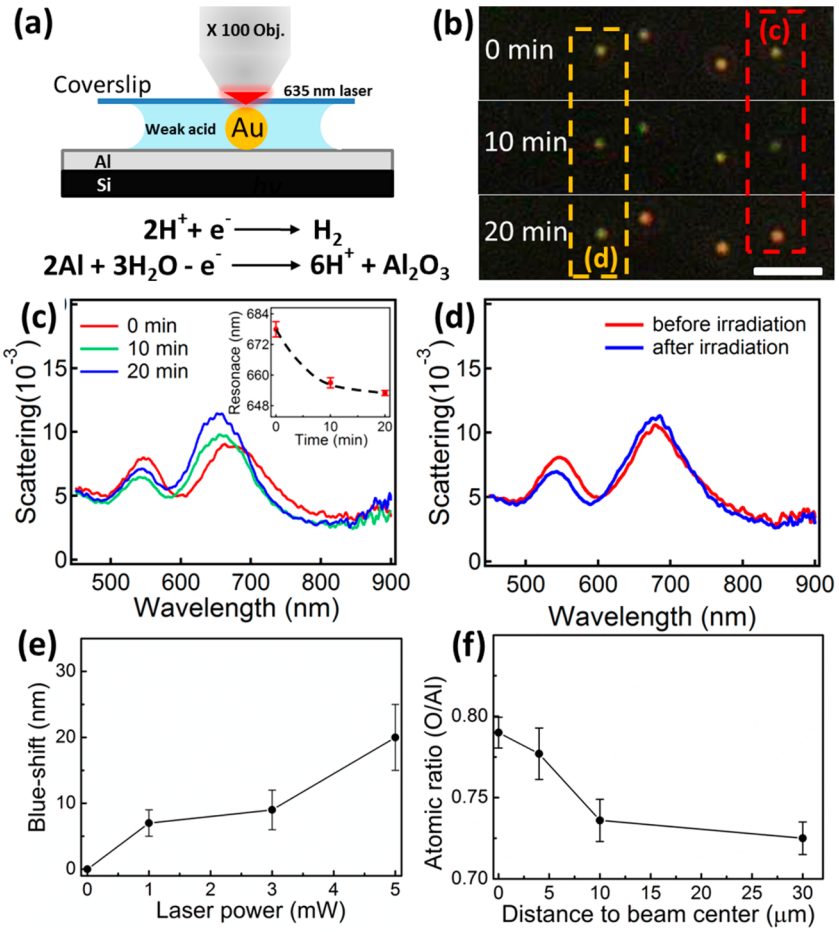

Figure 5. (a) Schematic illustration of the setup for *in situ* observation of Au NPs on Al mirror under laser (635 nm, 5 mW) irradiation and potential plasmon induced oxidation mechanism (b) Dark field images of Au NPs on Al mirror immersed in 4-ABA solution at 0, 10, and 20 min irradiation. Red dashed frame highlights the irradiated Au NPs, while the orange dashed frame indicates the nonirradiated Au NPs that is far from center of the beam spot. Scale bars are 5 μm. (c) Scattering spectra of the Au NP highlighted in panel b with a red dashed frame at different irradiation times. (d) Scattering spectra of the Au NP highlighted in panel (b) with an orange dashed frame before and after irradiation. (e) Change of blue-shift with the irradiation power. (f) Change of atomic ratio (O/Al) at different spots away from irradiation center.

different gap sizes. These BEM simulations use a gap refractive index of 1.8. With increasing gap size from 1.5 to 3.0 nm (calibrated by XPS), the resonance peak in experiment blue-shifts from 692 to 644 nm, which shows excellent agreement with the simulations (Figure 4f).

An even more appealing oxidation technique is to locally oxidize Al with the assistance of photons. The Au-NP-on-Al-mirror samples were immersed in 4-aminobenzamidine dihydrochloride solution (4-ABA, 0.1M) under a coverslip and irradiated with a 5 mW 635 nm laser focused to a sub-μm spot (Figure 5a). The Au NPs were monitored by dark field microscopy during this laser irradiation process (Figure 5b), and a distinct green to red color change was observed for the irradiated NPoMs (red dashed frame) with no change seen for nonirradiated controls (orange dashed frame). The corresponding scattering spectra of the irradiated NPoM were blue-shifted from 678 to 653 nm (Figure 5c) with no shift observed for the nonirradiated ones nearby (Figure 5d). This shows photoinduced oxidation can thus *locally* modify specific target NPoMs while leaving neighbors unaffected, for instance enabling the tweaking of an array of NPoM plasmon resonances to match a desired sensing laser wavelength. The blue shift observed is seen to saturate around 650 nm, possibly because of the blocking of H^+ ions when thicker and denser Al_2O_3 layers are formed. From the simulation in Figure 4f, we estimate the thickness of Al_2O_3 is increased to 3 nm after irradiation. With neutralized 4-ABA solution or NH_4Cl solution, no blue shift is observed (Supporting Information Figure S10a, c), indicating that the redox reaction requires sufficient protons to progress. With weaker acids such as AcOH, irradiation lead to smaller blue shifts (of 10 nm) of the longitudinal modes of Au NPoMs (Supporting Information Figure S10b), which further confirms the involvement of protons in the reduction process. By contrast, using stronger acids such as HCl, the longitudinal mode red-shifts instead after irradiation (Supporting Information Figure S10d), possibly because of etching of Al_2O_3 layer,[29] which leads to stronger coupling. Further irradiation at

elevated temperatures however leads to competing etching of the Al, and hence eventually blue-shifts (Supporting Information Figure S11). Irradiating with different laser powers we find blue shifts proportional to the magnitude of the irradiation power (Figure 5e and Supporting Information Figure S12). A careful investigation of the elemental composition at different locations around the irradiation spot (Supporting Information Figure S13) shows the atomic ratio of O to Al decreases at increasing distances from the irradiation center (Figure 5f), which provides additional evidence for the photoinduced oxidation mechanism. Direct photochemistry or plasmon heating are both unlikely since the former requires higher photon energies in the UV,[30] while the latter is not supported by thermal heating control experiments where no blue shift was observed (Supporting Information Figure S14). We note that although direct photon-induced oxidation of Al should not be favorable, the electron−hole pairs generated in the gap by the strongly coupled plasmons can trigger such redox processes.[31] The photoelectrons can reduce H^+ ions into H_2 and the holes can promote oxidation at the interface between Al and Al_2O_3. Thus, hot electron effects may play a role in the detailed mechanism behind this light-activated tuning.[32−35]

This work proves that controlled oxidation of Al in the NPoM geometry is highly effective in producing tuning of the coupled dipolar plasmon. Since the spectral peak positions can be determined with an accuracy of a few nm, the calibrated thickness of oxide can be tracked over sub-nm thickness changes, over areas of a few square nanometers set by the lateral field extent of the gap plasmon ($\sim(Rd)^{1/2}$). Our work shows how plasmonics can be used to study the subtle materials chemistry of surface contamination, transformation and etching in real environmental conditions. Spectral measurements are straightforward and clearly reveal surface modifications which are very hard to study with more traditional materials characterization such as EDX or XPS. We note that combining our approach with Al NPs would allow access to tight plasmonic confinement in the UV spectral region, suited for enhanced biomolecular sensing.

CONCLUSIONS

In conclusion, we have investigated the Au NP on Al mirror system which, because of the controlled oxidation of Al, enables tuning of the plasmonic coupling strength. We investigated different sized Au NPs on both Al mirrors and on Si substrates to confirm the significant coupling between Au NPs and Al metal. Tuning of the plasmon coupling of (Au)NPoM(Al) constructs was achieved in four distinct ways. Electrochemical oxidation of Al films was used to monitor *in situ* the change of the coupling under dark field microscopy. The scattering colors and spectra shift convincingly as electrochemical oxidation proceeds. Several other means of oxidation of Al films either by thermal annealing or oxygen plasma treatments, both show corresponding blue shifts of the resonance peak. Simulations support these trends and show that in this situation the scattering intensity is enhanced as the gap sizes increase after oxidation. Finally, we show a selective photo-oxidation approach, which locally oxidizes the Al underneath specific Au NPs. Similar controlled blue shifts of the longitudinal mode are observed, indicating thickening of the Al_2O_3 layer. The Au NP on Al mirror construct is used here as a specific example of a much more general approach for facile tuning of plasmonic coupling through surface chemistry, but it also deepens our understanding of the NPoM geometry. We note the suitability to extend this work to other families of reactive metals including Ag and Cu.

METHODS

Preparation of Au NPoM(Al) Nanostructures. Al films (50 nm) were thermally evaporated onto a clean silicon wafer with e-beam evaporation (Lesker) at a rate of 1 A/s. Aqueous solutions of Au NPs with different sizes (obtained from BBI) were drop-cast onto the Al substrate for 5 min, followed by blowing dry under nitrogen. Nanoparticles were sufficiently far apart to not interact spectrally or chemically.

Oxidation of Al Layer. Four different approaches were applied to oxidize the Al layer. The Al films were oxidized *via* oxygen plasma (100 W, O_2 flow rate 0.5 sccm, vacuum 3 mTorr) for different durations (5, 10, 20 min). The Al films were thermally oxidized in a tube furnace for 10 min under atmosphere at different annealing temperatures (450, 500, and 550 °C). The Al films were electrochemically oxidized while monitoring dark field microscopy. The setup is schematically shown in Figure 2a. The Al substrate was wet with 0.1 M AcOH (electrolyte) and covered with a glass coverslip. A two electrode system is employed to electrochemically oxidize the Al substrate. A thin Pt wire (0.2 mm) is used as a counter electrode, fixed to the Al substrate by double sided tape which functions as an insulator. A drop of AcOH was injected onto the Al films to immerse the Pt electrode through capillary forces, and the Al film functioned as the anode for electrochemical oxidation. A constant voltage of 4 V is applied to the substrate through a potentiostat (Ivium CompactStat). The Al films were photo-oxidized *via* laser irradiation. The setup is schematically shown in Figure 5a. The Al substrate was wet with 0.1 M 4-aminobenzamidine (4-ABA) dihydrochloride aqueous solution and covered with a glass coverslip. The Au NPs on the Al substrate were irradiated by a 635 nm laser with power of 5 mW for 20 min focused through an NA 0.80 dark field objective. Throughout, Au NPs on the Al film were monitored with dark field microscopy and the scattering spectra were recorded during the complete oxidation process.

Characterizations. The surface morphology of the Au NPs on the Al films was characterized with SEM (Zeiss, 1530VP) at an accelerating voltage of 5 kV, while EDX elemental analysis was carried out with 15 kV. Optical dark-field images were captured in an Olympus BX51 upright microscope using a 100× dark field objective (Olympus LMPLFLN-BD, NA 0.8). Scattered light from single NPs was collected through a confocal 50 μm optical fiber and sent to an Ocean Optics spectrometer (QE65000) for spectral analysis. A standard diffuser is used as a reference to

normalize white light scattering. The spectra obtained were from 20 randomly selected nanoparticles, which were averaged and statistically analyzed. The X-ray Photoemission Spectroscopy (XPS, ESCALAB 250Xi) for the composition of the Al films was carried out in depth mode. Specifically, the XPS for elements of Al and O were measured with accumulation of 5 times. Then a focused ion beam (500 V) was applied to mill away the surface layer of Al films at a rate of 0.05 nm/s for 10 s, followed by another cycle of XPS analysis of the films surface. Such cycles was proceeded for 8 levels to ensure reaching the depth of bulk Al.

Simulations. Simulations were performed using BEMAX, a boundary element solver.[36] The Al_2O_3 layer was modeled as a sheet of constant refractive index (n = 1.8) on top of a bulk Aluminum surface, while a 100 nm AuNP was placed on top. The dielectric functions were taken from Johnson and Christy. A broadband plane wave source was chosen for excitation, incident at an angle of 58° to account for the numerical aperture of NA = 0.85 in the experiments. A grid of 1 nm size was used in the gap region and the maximum of the near-field intensity in the gap between AuNP and Au surface was extracted for each spectral position. The thickness of the dielectric Al_2O_3 layer was varied between 0.5 and 5 nm and the near-field enhancement was analyzed to determine the wavelength of the plasmon resonance.

Conflict of Interest: The authors declare no competing financial interest.

Supporting Information Available: Statistics of scattering spectra, SEM and EDX analysis, and XPS in depth analysis. The Supporting Information is available free of charge on the ACS Publications website at DOI: 10.1021/acsnano.5b01283. All figure data of this paper can be found at http://www.repository.cam.ac.uk/handle/1810/247600.

Acknowledgment. We acknowledge financial support from EPSRC grants EP/G060649/1 and EP/I012060/1 and ERC grant LINASS 320503. We especially thank Christos Tserkezis and Javier Aizpurua for providing additional simulations and many helpful discussions.

REFERENCES AND NOTES

1. Halas, N. J.; Lal, S.; Chang, W.-S.; Link, S.; Nordlander, P. Plasmons in Strongly Coupled Metallic Nanostructures. *Chem. Rev.* **2011**, 3913–3961.
2. Jones, M. R.; Osberg, K. D.; Macfarlane, R. J.; Langille, M. R.; Mirkin, C. A. Templated Techniques for the Synthesis and Assembly of Plasmonic Nanostructures. *Chem. Rev.* **2011**, *111*, 3736–3827.
3. Giannini, V.; Fernández-Domínguez, A. I.; Heck, S. C.; Maier, S. A. Plasmonic Nanoantennas: Fundamentals and Their Use in Controlling the Radiative Properties of Nanoemitters. *Chem. Rev.* **2011**, *111*, 3888–3912.
4. Wadell, C.; Syrenova, S.; Langhammer, C. Plasmonic Hydrogen Sensing with Nanostructured Metal Hydrides. *ACS Nano* **2014**, *8*, 11925–11940.
5. Grzelczak, M.; Liz-Marzan, L. M. Colloidal Nanoplasmonics: From Building Blocks to Sensing Devices. *Langmuir* **2013**, *29*, 4652–4663.
6. Mock, J. J.; Hill, R. T.; Degiron, A.; Zauscher, S.; Chilkoti, A.; Smith, D. R. Distance-Dependent Plasmon Resonant Coupling between a Gold Nanoparticle and Gold Film. *Nano Lett.* **2008**, *8*, 2245–2252.
7. Zhou, W.; Dridi, M.; Suh, J. Y.; Kim, C. H.; Co, D. T.; Wasielewski, M. R.; Schatz, G. C.; Odom, T. W. Lasing Action in Strongly Coupled Plasmonic Nanocavity Arrays. *Nat. Nano* **2013**, *8*, 506–511.
8. Shen, Y.; Zhou, J.; Liu, T.; Tao, Y.; Jiang, R.; Liu, M.; Xiao, G.; Zhu, J.; Zhou, Z.-K.; Wang, X.; et al. Plasmonic Gold Mushroom Arrays with Refractive Index Sensing Figures of Merit Approaching the Theoretical Limit. *Nat. Commun.* **2013**, *4*, 2381.
9. Ritchie, R. H.; Arakawa, E. T.; Cowan, J. J.; Hamm, R. N. Surface-Plasmon Resonance Effect in Grating Diffraction. *Phys. Rev. Lett.* **1968**, *21*, 1530–1533.
10. Lucas, B. D.; Kim, J.-S.; Chin, C.; Guo, L. J. Nanoimprint Lithography Based Approach for the Fabrication of Large-Area, Uniformly-Oriented Plasmonic Arrays. *Adv. Mater.* **2008**, *20*, 1129–1134.
11. Li, L.; Hutter, T.; Steiner, U.; Mahajan, S. Single Molecule SERS and Detection of Biomolecules with a Single Gold Nanoparticle on a Mirror Junction. *Analyst.* **2013**, *138*, 4574–4578.
12. Taylor, R. W.; Benz, F.; Sigle, D. O.; Bowman, R. W.; Bao, P.; Roth, J. S.; Heath, G. R.; Evans, S. D.; Baumberg, J. J. Watching Individual Molecules Flex within Lipid Membranes Using SERS. *Sci. Rep.* **2014**, *4*, 5940.
13. Li, L.; Hutter, T.; Finnemore, A. S.; Huang, F. M.; Baumberg, J. J.; Elliott, S. R.; Steiner, U.; Mahajan, S. Metal Oxide Nanoparticle Mediated Enhanced Raman Scattering and Its Use in Direct Monitoring of Interfacial Chemical Reactions. *Nano Lett.* **2012**, *12*, 4242–4246.
14. Sigle, D. O.; Hugall, J. T.; Ithurria, S.; Dubertret, B.; Baumberg, J. J. Probing Confined Phonon Modes in Individual CdSe Nanoplatelets Using Surface-Enhanced Raman Scattering. *Phys. Rev. Lett.* **2014**, *113*, No. 087402.
15. Chen, S.-Y.; Mock, J. J.; Hill, R. T.; Chilkoti, A.; Smith, D. R.; Lazarides, A. A. Gold Nanoparticles on Polarizable Surfaces as Raman Scattering Antennas. *ACS Nano* **2010**, *4*, 6535–6546.
16. Hill, R. T.; Mock, J. J.; Urzhumov, Y.; Sebba, D. S.; Oldenburg, S. J.; Chen, S.-Y.; Lazarides, A. A.; Chilkoti, A.; Smith, D. R. Leveraging Nanoscale Plasmonic Modes to Achieve Reproducible Enhancement of Light. *Nano Lett.* **2010**, *10*, 4150–4154.
17. Mertens, J.; Shi, Y.; Molina-Sánchez, A.; Wirtz, L.; Yang, H. Y.; Baumberg, J. J. Excitons in a Mirror: Formation of "Optical Bilayers" Using MoS_2 Monolayers on Gold Substrates. *Appl. Phys. Lett.* **2014**, *104*, No. 191105.
18. Mertens, J.; Eiden, A. L.; Sigle, D. O.; Huang, F.; Lombardo, A.; Sun, Z.; Sundaram, R. S.; Colli, A.; Tserkezis, C.; Aizpurua, J.; et al. Controlling Subnanometer Gaps in Plasmonic Dimers Using Graphene. *Nano Lett.* **2013**, *13*, 5033–5038.
19. Hu, M.; Ghoshal, A.; Marquez, M.; Kik, P. G. Single Particle Spectroscopy Study of Metal-Film-Induced Tuning of Silver Nanoparticle Plasmon Resonances. *J. Phys. Chem. C* **2010**, *114*, 7509–7514.
20. Lumdee, C.; Toroghi, S.; Kik, P. G. Post-Fabrication Voltage Controlled Resonance Tuning of Nanoscale Plasmonic Antennas. *ACS Nano* **2012**, *6*, 6301–6307.
21. Sigle, D. O.; Perkins, E.; Baumberg, J. J.; Mahajan, S. Reproducible Deep-UV SERS on Aluminum Nanovoids. *J. Phys. Chem. Lett.* **2013**, *4*, 1449–1452.
22. Sigle, D. O.; Mertens, J.; Herrmann, L. O.; Bowman, R. W.; Ithurria, S.; Dubertret, B.; Shi, Y.; Yang, H. Y.; Tserkezis, C.; Aizpurua, J.; Baumberg, J. J. Monitoring Morphological Changes in 2D Monolayer Semiconductors Using Atom-Thick Plasmonic Nanocavities. *ACS Nano* **2015**, *9*, 825–830.
23. Saif, M. T. A.; Zhang, S.; Haque, A.; Hsia, K. J. Effect of Native Al_2O_3 on the Elastic Response of Nanoscale Al Films. *Acta Mater.* **2002**, *50*, 2779–2786.
24. Antula, J. Thickness Study of Thermally Oxidized and Anonized Thin Al_2O_3 Films. *Thin Solid Films* **1969**, *3*, 183–188.
25. Olefjord, I.; Nylund, A. Surface Analysis of Oxidized Aluminium. 2. Oxidation of Aluminium in Dry and Humid Atmosphere Studied by ESCA, SEM, SAM, and EDX. *Surf. Interface Anal.* **1994**, *21*, 290–297.
26. Yamamoto, N.; Ohtani, S.; García de Abajo, F. J. Gap and Mie Plasmons in Individual Silver Nanospheres near a Silver Surface. *Nano Lett.* **2011**, *11*, 91–95.
27. Parsons, R. *Effect of an Oxygen Plasma on Uncoated Thin Aluminum Reflecting Films*; Gulino, D. A., Ed.; National Aeronautics and Space Administration: Washington, DC, 1987.
28. Baran, J. D.; Grönbeck, H.; Hellman, A. Mechanism for Limiting Thickness of Thin Oxide Films on Aluminum. *Phys. Rev. Lett.* **2014**, *112*, No. 146103.
29. Weirauch, D. F.; Kung, R. The Hydrothermal Growth of Al_2O_3 in HCl Solutions. *J. Cryst. Growth* **1973**, *19*, 139–140.
30. Chang, C.-L.; Engelhard, M. H.; Ramanathan, S. Superior Nanoscale Passive Oxide Layers Synthesized under

Photon Irradiation for Environmental Protection. *Appl. Phys. Lett.* **2008**, *92*, No. 263103.
31. Lumdee, C.; Yun, B.; Kik, P. G. Gap-Plasmon Enhanced Gold Nanoparticle Photoluminescence. *ACS Photonics* **2014**, *1*, 1224–1230.
32. Mukherjee, S.; Libisch, F.; Large, N.; Neumann, O.; Brown, L. V.; Cheng, J.; Lassiter, J. B.; Carter, E. A.; Nordlander, P.; Halas, N. J. Hot Electrons Do the Impossible: Plasmon-Induced Dissociation of H_2 on Au. *Nano Lett.* **2013**, *13*, 240–247.
33. Marchuk, K.; Willets, K. A. Localized Surface Plasmons and Hot Electrons. *Chem. Phys.* **2014**, *445*, 95–104.
34. Wu, K.; Rodríguez-Córdoba, W. E.; Yang, Y.; Lian, T. Plasmon-Induced Hot Electron Transfer from the Au Tip to CdS Rod in CdS-Au Nanoheterostructures. *Nano Lett.* **2013**, *13*, 5255–5263.
35. Clavero, C. Plasmon-Induced Hot-Electron Generation at Nanoparticle/Metal-Oxide Interfaces for Photovoltaic and Photocatalytic Devices. *Nat. Photonics* **2014**, *8*, 95–103.
36. García de Abajo, F. J.; Howie, A. Relativistic Electron Energy Loss and Electron-Induced Photon Emission in Inhomogeneous Dielectrics. *Phys. Rev. Lett.* **1998**, *80*, 5180–5183.